High-field effective linewidth and eddy current losses in moderate conductivity single-crystal M-type barium hexagonal ferrite disks at 10–60 GHz

John R. Truedson, Kevin D. McKinstry, Pavel Kabos, and Carl E. Patton
Department of Physics, Colorado State University, Fort Collins, Colorado 80523

(Received 1 March 1993; accepted for publication 5 May 1993)

The losses associated with the high-field tail region of the ferromagnetic resonance (FMR) absorption curve were investigated at 10, 19, 35, and 60 GHz for 0.10–1.75-mm-thick *c*-plane circular disks of flux-grown single-crystal M-type barium ferrite materials. A conventional high-field effective linewidth analysis of the data yielded an effective linewidth which increased with the square of the disk thickness and linearly with frequency, dependencies which indicate a predominant eddy current loss process. Based on these results, an eddy current loss analysis of the tail region was done, based on the insulator FMR response and eddy current losses driven by the FMR response. This analysis leads to a new noninvasive technique for the determination of the microwave conductivity in moderate conductivity ferrites. One obtains the conductivity from an appropriate analysis of the FMR absorption tail in the same way that analysis of the magnetic loss tail yields a high-field effective linewidth. Based on this technique, the microwave conductivity of these flux-grown barium ferrite single-crystal materials was determined as a function of frequency and found to increase linearly from $0.033 \pm 0.004\ \Omega^{-1}\ \mathrm{cm}^{-1}$ at 10 GHz to $0.10 \pm 0.02\ \Omega^{-1}\ \mathrm{cm}^{-1}$ at 60 GHz. These results are consistent with a measured dc conductivity of 0.03–0.05 $\Omega^{-1}\ \mathrm{cm}^{-1}$.

I. INTRODUCTION

Off-resonance effective linewidth analysis techniques[1] to characterize the microwave losses in magnetic materials have been used to study microstructure related two-magnon relaxation processes[2,3] and to determine intrinsic losses in inhomogeneous materials.[4] The technique has been used recently to study microwave losses in hexagonal ferrite materials.[5–8] In the hexagonal ferrite work described in Refs. 5 and 8 the technique was extended to the determination of effective linewidth parameters in situations where the actual ferromagnetic resonance (FMR) peak is not accessible, due to the combination of large anisotropy fields and a relatively low microwave frequency.

The work in Ref. 8 was on thin *c*-plane disks of single-crystal M-type barium ferrite. One of the initially surprising results of that work was an observed increase in the effective linewidth which was proportional to the square of the disk thickness. This quadratic dependence indicated a possible eddy current origin for the losses. The pure Ba-M-type materials used for the work were found to have moderate resistivities in the 1–20 Ω cm range. Such resistivity values were determined to be quantitatively consistent with the observed losses.

The objective of the present work is to further explore the eddy current origins of the microwave and millimeter wave losses and off-resonance effective linewidth in these moderate conductivity Ba-M-type hexagonal ferrite single-crystal materials. In the first phase of the work the measurements reported in Ref. 8 for 10 GHz were extended to 19, 35, and 60 GHz. The standard insulator effective linewidth parameter is found to scale with the square of the disk thickness at all measurement frequencies and to scale linearly with frequency. In the second phase of the work, a simple model first reported by Smith[9] and developed by Schlömann, Kohane, and Green[10] to determine the contribution of eddy current losses to the FMR linewidth in metal films was adapted to the off-resonance problem and used to calculate the effect of eddy current losses on the FMR tail response for perpendicularly magnetized barium ferrite single-crystal *c*-plane thin disk samples. This eddy current tail (ECT) response analysis leads to a simple fitting procedure similar to that used for the high-field effective linewidth in Ref. 8. The ECT analysis, however, applied to the ensemble of data for different Ba-M disk thicknesses, yields a direct empirical determination of the microwave conductivity. The microwave conductivity increases linearly with frequency and extrapolates to dc values at low frequency.

The analyses below and all magnetic parameters are given in cgs units. The conductivity σ in the cgs system has units of s^{-1}. Numerical values of σ, where pertinent, are given in the more common mixed units of $\Omega^{-1}\ \mathrm{cm}^{-1}$.

II. MATERIALS, PROPERTIES, AND MICROWAVE MEASUREMENTS

The objective of the work presented here was to investigate the effects of eddy currents on the off-resonance microwave and millimeter wave losses in Ba-M-type hexagonal ferrite. Eddy current losses generally show characteristic sample size effects. For this reason, and based on the earlier results in Ref. 8, the high-frequency measurements were made on carefully prepared, well-characterized disk-shaped samples of varying thickness. These measurements were then analyzed by two methods:

 0021-8979/93/74(4)/2705/14/$6.00 © 1993 American Institute of Physics

Downloaded 26 Dec 2001 to 129.82.140.114. Redistribution subject to AIP license or copyright, see http://ojps.aip.org/japo/japcr.jsp

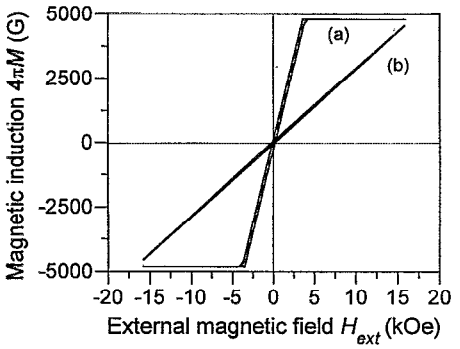

FIG. 1. Easy and hard direction hysteresis loop plots of magnetic induction $4\pi M$ vs static external magnetic field H_{ext} for a single-crystal barium ferrite c-plane disk with diameter $D=3.0$ mm and thickness $T=0.33$ mm. For the easy direction hysteresis loop shown by curve (a), the magnetic field is along the c axis and easy direction perpendicular to the disk plane. For the hard direction hysteresis loop shown by curve (b), the magnetic field is applied in the plane of the disk.

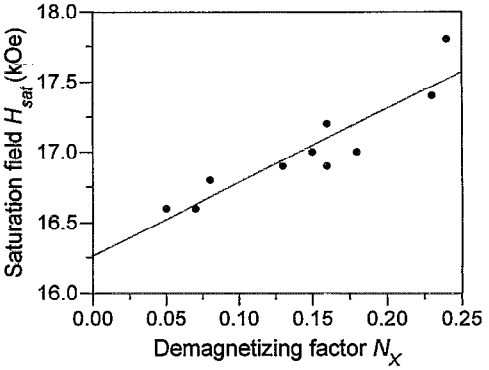

FIG. 2. Plot of the hard direction hysteresis loop extrapolated saturation field H_{sat} vs disk in-plane demagnetizing factor N_x. The data are for several 3-mm-diam barium ferrite disks of different thicknesses. The solid line represents a straight-line best fit to the data.

(i) the standard high-field effective linewidth technique from Ref. 8, and (ii) a new effective conductivity analysis procedure.

The barium ferrite single crystals were prepared at Purdue University by a flux-melt growth method and characterized by x-ray diffraction, polarized light optical microscopy, scanning electron microscopy, and inductively coupled plasma emission spectroscopy.[11] Lapidary techniques were used to fabricate thin c-plane disks. The disks were polished to a surface smoothness of about 1 μm. The finished disk thicknesses ranged from 0.10 to 1.75 mm. Disk diameters ranged from about 3 mm for the 10 GHz measurements to 0.5 mm for the 60 GHz measurements. Smaller sample volumes were needed for the higher frequencies because of filling factor and microwave cavity loading effects.

The static magnetic properties of the larger disk samples were characterized by vibrating sample magnetometry. Hysteresis curves of the magnetic induction $4\pi M$ versus static external magnetic field H_{ext} were measured for both easy direction magnetic fields applied perpendicular to the disk plane and hard direction fields applied in the disk plane. Values for the saturation induction $4\pi M_s$ and uniaxial anisotropy field H_A were determined from these measurements. A typical pair of hard and easy direction hysteresis curves is shown in Fig. 1 for a 0.33-mm thick, 3.0-mm-diam disk. The easy direction hysteresis curve, labeled (a) in Fig. 1, was obtained with the magnetic field applied along the crystal c axis and perpendicular to the disk plane. The hard direction hysteresis curve for in-plane fields, labeled (b) in the figure, was measured with the field applied in the plane of the disk. The easy direction hysteresis curves for all samples saturate for fields on the order of 3 kOe or so. The saturation induction $4\pi M_s$ determined from saturation measurements on ten 3-mm-diam samples ranging in thickness from 0.19 to 1.75 mm was determined to be 4.73 ± 0.11 kG.

The hard direction hysteresis curves were used to determine the anisotropy field H_A. This anisotropy field is defined by the relation $H_A=2K_u/M_s$, where K_u is the usual uniaxial anisotropy energy density parameter in erg/cm^3. These curves, as evident from curve (b) in Fig. 1, were generally linear in field for the range of fields available, up to about 15 kOe or so. These curves were extrapolated to the easy direction saturation $4\pi M_s$ values for each sample measured to determine values of the saturation field H_{sat} in each case. These H_{sat} values ranged from 16.6 to 17.9 kOe. Thicker disks generally had larger H_{sat} values. It is clear, therefore, that these saturation fields do not correspond directly to the theoretical saturation field for very thin films, $H_A-4\pi M_s$.

The anisotropy field H_A was obtained by plotting the measured H_{sat} values versus the disk in-plane demagnetizing factor N_x and extrapolating the data to the value of H_{sat} limit at $N_x=0$. This plot, along with the straight-line best fit to the data, is shown in Fig. 2. The N_x parameters were obtained from the disk sample dimensions, the ellipsoidal sample approximation, and the work of Osborn.[12] The extrapolated value of H_{sat} at $N_x=0$ is 16.3 ± 0.3 kOe. This value is at the lower end of the range of H_A values usually cited for barium ferrite.[13]

The above procedure can be justified on the basis of a simple domain rotation model. For a disk made up of narrow stripe domains, it can be argued that the hard direction saturation field H_{sat} value should vary according to

$$H_{sat}=H_A+4\pi M_s N_x, \tag{1}$$

where N_x is the sample demagnetizing factor for the hard in-plane field direction. Equation (1) and all equations and analyses below are based on cgs units. The N_z demagnetizing factor for the direction perpendicular to the disk plane does not appear because for alternating stripe domains aligned parallel to the applied hard direction in-plane field the effective demagnetizing factor in this direction is zero. The value of H_{sat} varies linearly with the demagnetizing factor N_x and, in the limit of zero disk thickness, is equal to the anisotropy field H_A. The dependence indicated in Eq. (1) is in agreement with the data and the fit in Fig. 2. The

Downloaded 26 Dec 2001 to 129.82.140.114. Redistribution subject to AIP license or copyright, see http://ojps.aip.org/japo/japcr.jsp

slope of the fitted line in the figure is 4.8 ± 1.1 kG, equal to the measured value of $4\pi M_s$ from the saturated easy direction hysteresis curves.

Microwave and millimeter wave magnetic loss and dispersion measurements were made for easy direction fields ranging from well above the ferromagnetic resonance field position, if accessible at the operating frequency, up to 16 kOe or so. These measurements were made at nominal frequencies of 10.0, 19.3, 35.3, and 60.5 GHz with dedicated high Q transmission cavity microwave and millimeter wave spectrometers at the listed frequencies. The basic measurement was of cavity Q and cavity frequency for a cylindrical TE_{011} high-Q cavity as a function of the static external magnetic field. Specially designed cavities were used for each operating frequency. The empty cavity Q values were 25 000, 16 000, 14 000, and 10 000 at the respective frequencies listed above. The measurement procedure was the same as used by Patton and Kohane,[14] adapted to modern instrumentation, data acquisition, and Q-measurement techniques.[15,16] In a typical cavity measurement, a disk sample is mounted in the center of the TE_{011} cylindrical microwave cavity which is centered in the gap of an electromagnet. The sample is mounted such that the disk normal is perpendicular to the cavity axis. The static external field H_{ext} is applied along this normal direction, parallel to the hexagonal crystal c-axis direction. The linearly polarized microwave or millimeter wave magnetic field is in the disk plane. The cavity resonance frequency ω and cavity Q are then measured as a function of the static external magnetic field.

Typical measurements of the cavity resonance frequency ω and quality factor Q versus static external magnetic field H_{ext} are shown in Fig. 3. The data shown are for the 10 GHz cavity and a 0.87-mm-thick, 3.0-mm-diam disk. The increase in frequency with field shown in Fig. 3(a) corresponds to the high-field FMR dispersion tail. The increase in Q with field shown in Fig. 3(b) corresponds to the FMR loss tail at high field. Both tails appear inverted relative to the usual way of plotting FMR curves. For the 10 GHz excitation frequency applicable to Fig. 3, the theoretical FMR peak position occurs at about -8 kOe and is inaccessible for the positive field values available in the experiment. Only the tail responses are accessible at 10 GHz. It is important to note that the changes in Q and frequency ω with H_{ext} in this tail region are small. For the data in Fig. 3, the cavity resonance frequency increase from 5 to 10 kOe is about 400 kHz, a change of 0.004%. The cavity Q factor increases from about 12 700 at 5 kOe to about 13 300 at 10 kOe, less than a 5% change. The small changes in these parameters over such a relatively wide field range are indicative of the small changes in the microwave susceptibility far from FMR. As will be evident from the discussion in Secs. III and IV, these Q values are significantly lower than the empty cavity Q, Q_{emp}, because of eddy current losses in the barium ferrite disk sample. The value of Q_{emp} for the 10 GHz cavity is about 25 000. This difference is responsible, in part, for the difference in the cavity calibration parameters from those

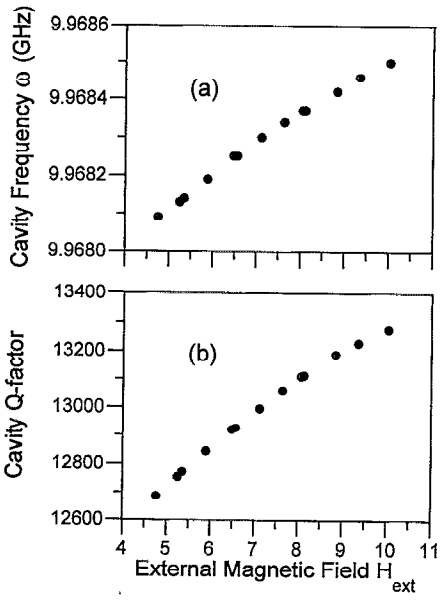

FIG. 3. Plots of (a) cavity resonance frequency ω and (b) cavity Q factor vs static external magnetic field H_{ext} for a barium ferrite disk of diameter $D=3.0$ mm and thickness $T=0.87$ mm in the center of a 10 GHz TE_{011} cylindrical cavity. The static field was perpendicular to the disk plane and the cavity microwave field was in plane.

calculated from microwave cavity perturbation theory. This point is discussed in Sec. III.

This type of microwave data on ferrite samples with a well-defined uniform mode resonance response can be used to determine a high-field far-from-resonance loss parameter, usually expressed as a high-field effective linewidth.[3,4] For the moderate conductivity barium ferrite materials of interest here, this high-field effective linewidth contains a significant eddy current loss contribution. In this situation the same data, in combination with a simple eddy current loss analysis and a modified high-field effective linewidth analysis technique, can be used to analyze the eddy current loss directly and determine the microwave conductivity of the ferrite.

The high-field effective linewidth analysis technique is summarized in Sec. III, along with the results of the analysis for the barium ferrite samples described above. The effective linewidth approach is extended in Sec. IV to treat eddy current losses explicitly. This extended technique allows one to utilize the same basic data on cavity frequency and Q versus field for moderate conductivity materials to obtain the microwave conductivity from the high-field data.

III. EFFECTIVE LINEWIDTH ANALYSIS

The cavity measurements described in the previous section can be used to determine a far-from-resonance high-field effective linewidth loss parameter. This high-field effective linewidth is generally smaller than the conventional FMR linewidth and may be taken as a good indicator of the intrinsic microwave magnetic losses in many cases, without the contributions from two magnon scatter-

Downloaded 26 Dec 2001 to 129.82.140.114. Redistribution subject to AIP license or copyright, see http://ojps.aip.org/japo/japcr.jsp

ing and inhomogeneities which often broaden the actual FMR absorption peak. The technique is described in detail in Refs. 1–4. A recent modification of the technique for the determination of a single high-field effective linewidth parameter was summarized in Ref. 8. This section provides a full description of the technique and gives high-field effective (HFE) linewidth results for the thin disk barium ferrite materials at 10, 19, 35, and 60 GHz. It is important to keep in mind that the treatment presented in this section assumes that the pertinent losses that contribute to the tail of the FMR absorption curve are magnetic in origin. As indicated in Sec. I the predominant losses in the present materials are eddy current losses. The technique described in this section, however, is also a starting point for the eddy current tail (ECT) analysis developed in Sec. IV.

The starting point for the magnetic loss analysis is the connection between the microwave susceptibility tensor of the ferrite sample and measurable parameters. Consider a magnetic sample in the form of an ellipsoid of revolution about a z axis and magnetized to saturation in the z direction by an applied static external magnetic field H_{ext}. A uniform transverse x-y plane microwave field $\mathbf{h}(t)=\mathbf{h}e^{i\omega t}$ of amplitude $\mathbf{h}$ and frequency ω produces a dynamic magnetization response $\mathbf{m}(t)=\mathbf{m}e^{i\omega t}$, where $\mathbf{m}$ denotes the complex dynamic magnetization amplitude. In the low-power linear response limit, only the x and y components of $\mathbf{m}$, m_x and m_y, need be considered. This dynamic linear response can be written as

$$4\pi\begin{bmatrix} m_x \\ m_y \end{bmatrix}=4\pi\begin{bmatrix} \chi_{\text{mag}} & -i\kappa_{\text{mag}} \\ i\kappa_{\text{mag}} & \chi_{\text{mag}} \end{bmatrix}\mathbf{h}. \tag{2}$$

The susceptibility tensor components χ_{mag} and κ_{mag} can be separated into real and negative imaginary parts according to $\kappa_{\text{mag}}=\kappa'_{\text{mag}}-i\kappa''_{\text{mag}}$ and $\chi_{\text{mag}}=\chi'_{\text{mag}}-i\chi''_{\text{mag}}$. For a saturated ferrite ellipsoid of revolution with the static magnetic field along the z direction and axis of rotational symmetry, the susceptibility parameters $4\pi\chi'_{\text{mag}}$, $4\pi\chi''_{\text{mag}}$, $4\pi\kappa'_{\text{mag}}$, and $4\pi\kappa''_{\text{mag}}$ are given by

$$4\pi\chi'_{\text{mag}}=\frac{4\pi M_s H_0[H_0^2-(\omega/\gamma)^2]}{[H_0^2-(\omega/\gamma)^2]^2+H_0^2(\Delta H)^2}, \tag{3}$$

$$4\pi\chi''_{\text{mag}}=\frac{1}{2}\frac{4\pi M_s\Delta H[H_0^2+(\omega/\gamma)^2]}{[H_0^2-(\omega/\gamma)^2]^2+H_0^2(\Delta H)^2}, \tag{4}$$

$$4\pi\kappa'_{\text{mag}}=-\frac{4\pi M_s(\omega/\gamma)[H_0^2-(\omega/\gamma)^2]}{[H_0^2-(\omega/\gamma)^2]^2+H_0^2(\Delta H)^2}, \tag{5}$$

and

$$4\pi\kappa''_{\text{mag}}=-\frac{4\pi M_s\Delta H H_0(\omega/\gamma)}{[H_0^2-(\omega/\gamma)^2]^2+H_0^2(\Delta H)^2}. \tag{6}$$

The H_0 parameter in Eqs. (3)–(6) represents an effective stiffness field. For a barium ferrite thin disk magnetized to saturation by the external magnetic field H_{ext} perpendicular to the disk plane, H_0 is given by

$$H_0=H_{\text{ext}}+H_A-4\pi M_s(N_z-N_x). \tag{7}$$

The ΔH parameter in Eqs. (3)–(6) is the usual half-power ferromagnetic resonance linewidth, the field width at half-maximum of the FMR absorption curve of $4\pi\chi''_{\text{mag}}$ vs H_{ext} from Eqs. (4) and (7). The γ parameter denotes the absolute value of the gyromagnetic ratio for the exchange coupled $3d$ electrons which give rise to the net ferrite magnetization. In this work, γ will be taken as 1.76×10^7 rad/Oe s or 2.8 GHz/kOe, the value corresponding to an electron system with quenched orbital angular momentum and a Landé g factor $g=2$. This is an accurate approximation for barium ferrite.[13]

Ferromagnetic resonance (FMR) occurs when the condition $H_0=\omega/\gamma$ is satisfied and the resonance denominator in Eqs. (3)–(6) is minimized. This $H_0=\omega/\gamma$ resonance condition, Eq. (7), and the requirement that the external magnetic field at resonance be positive and sufficient to magnetize the sample to saturation lead to a minimum frequency for FMR in c-plane barium ferrite disks with a c-axis static field. For the barium ferrite parameters given in Sec. II, and demagnetizing factors $N_x\approx0$ and $N_z\approx1$ for a thin disk, this minimum FMR frequency is about 40 GHz. As will be evident from the procedure described below and the data presented at the end, of this section, it is possible to determine high-field effective linewidths from the tail response of the FMR, even for frequencies below this 40 GHz FMR cutoff frequency.

The $4\pi\chi'_{\text{mag}}$, $4\pi\chi''_{\text{mag}}$, $4\pi\kappa'_{\text{mag}}$, and $4\pi\kappa''_{\text{mag}}$ functions play different roles in the microwave response of a ferrite. The FMR absorption curve of microwave loss versus frequency or field follows the functional form of the $4\pi\chi''_{\text{mag}}$ response, in the form of a Lorentzian resonance with a half-width in field given by ΔH, as discussed above. For the measurement process of Sec. II with a linearly polarized microwave field, the observed change in the cavity Q with field and the corresponding FMR absorption curve is directly connected to $4\pi\chi''_{\text{mag}}$. The change in cavity frequency with field and the corresponding FMR dispersion curve is directly connected to $4\pi\chi'_{\text{mag}}$. The $4\pi\kappa'_{\text{mag}}$, and $4\pi\kappa''_{\text{mag}}$ response functions play no role in the FMR response for a linearly polarized microwave field excitation. These functions will be important, however, for the eddy current analysis of the following section.

One reason for the development of the effective linewidth concept is the fact that the losses that determine the FMR linewidth and the actual values of the microwave susceptibility components at any given field can be field dependent. The ΔH parameter in the above equations, which is generally taken as a constant in conventional FMR analyses, then becomes a field-dependent quantity, $\Delta H(H_{\text{ext}})$. In the context of this work, the value of $\Delta H(H_{\text{ext}})$ at very high fields, well above the FMR field, represents an important limit. In this limit, the spin-wave band is shifted to frequencies well above the operating frequency and the field-dependent linewidth is representative of the losses in the absence of two magnon scattering relaxation processes. This high-field effective linewidth ΔH_{HFE} can then be taken as a field-independent constant which represents the intrinsic losses in the material. As will be discussed below, data on cavity frequency and cavity Q

Downloaded 26 Dec 2001 to 129.82.140.114. Redistribution subject to AIP license or copyright, see http://ojps.aip.org/japo/japcr.jsp

versus static external magnetic field in the high-field region, corresponding to the high-field tail of the FMR absorption curve, allow one to determine the high-field effective linewidth ΔH_{HFE} with high accuracy. In Sec. IV, a modification of the same procedure is developed which allows the direct noninvasive determination of microwave conductivity for moderate conductivity ferrite materials in general and barium ferrite in particular.

In the high-field regime the condition $H_0 \gg \Delta H$ is satisfied and the $4\pi\chi'_{\mathrm{mag}}$ and $4\pi\chi''_{\mathrm{mag}}$ response functions can be written in a simplified form. In this limit, the expressions Eq. (3) for $4\pi\chi'_{\mathrm{mag}}$ and Eq. (4) for $4\pi\chi''_{\mathrm{mag}}$ may be replaced by the $4\pi\chi'_{\mathrm{HFE}}$ and $4\pi\chi''_{\mathrm{HFE}}$ expressions given below (the HFE subscript stands for "high-field effective" in the high-field regime):

$$4\pi\chi'_{\mathrm{HFE}}=\frac{4\pi M_s H_0}{H_0^2-(\omega/\gamma)^2}, \tag{8}$$

$$4\pi\chi''_{\mathrm{HFE}}=\frac{1}{2}\frac{4\pi M_s \Delta H_{\mathrm{HFE}}[H_0^2+(\omega/\gamma)^2]}{[H_0^2-(\omega/\gamma)^2]^2}. \tag{9}$$

Note that the $4\pi\chi'_{\mathrm{HFE}}$ expression, compared to $4\pi\chi'_{\mathrm{mag}}$, now contains no linewidth parameter. Note also that the $4\pi\chi''_{\mathrm{HFE}}$ expression, compared to $4\pi\chi''_{\mathrm{mag}}$, now contains a linewidth parameter only as the multiplicative ΔH_{HFE} factor in the numerator. As indicated above, in this high-field regime the intrinsic linewidth is denoted by the high-field effective linewidth parameter ΔH_{HFE}.

The corresponding high-field limit expressions for $4\pi\kappa'_{\mathrm{mag}}$, and $4\pi\kappa''_{\mathrm{mag}}$ are given below:

$$4\pi\kappa'_{\mathrm{HFE}}=-\frac{4\pi M_s(\omega/\gamma)}{H_0^2-(\omega/\gamma)^2}, \tag{10}$$

$$4\pi\kappa''_{\mathrm{HFE}}=-\frac{4\pi M_s \Delta H_{\mathrm{HFE}} H_0(\omega/\gamma)}{[H_0^2-(\omega/\gamma)^2]^2}. \tag{11}$$

These parameters are not needed for the high-field effective linewidth analysis; they are needed for the effective conductivity tail (ECT) analysis of the following section.

As indicated above, the real and negative imaginary terms in the diagonal component of the microwave susceptibility tensor give rise to experimentally observable changes in the frequency and Q of the TE_{011} cylindrical microwave cavity containing the appropriately positioned sample as the external magnetic field is changed. It is these changes that allow one to determine the high-field effective linewidth ΔH_{HFE}. The quantitative connections between these frequency and Q changes and the terms in $4\pi\chi_{\mathrm{mag}}$ or $4\pi\chi_{\mathrm{HFE}}$ are given from standard microwave cavity perturbation theory,[17]

$$\frac{\omega(H_{\mathrm{ext}})-\omega_N}{\omega(H_{\mathrm{ext}})}=-K_{\mathrm{cav}}4\pi\chi'_{\mathrm{HFE}}(H_{\mathrm{ext}}), \tag{12}$$

$$\frac{1}{Q(H_{\mathrm{ext}})}-\frac{1}{Q_N}=2K_{\mathrm{cav}}4\pi\chi''_{\mathrm{HFE}}(H_{\mathrm{ext}}). \tag{13}$$

In the above, the cavity Q and frequency ω, denoted by $Q(H_{\mathrm{ext}})$ and $\omega(H_{\mathrm{ext}})$, respectively, are shown explicitly as functions of the external field H_{ext}. As the field is changed and the susceptibility terms change, the cavity frequency and the Q also change. The susceptibility terms are also shown as explicit functions of H_{ext} by writing $\chi'_{\mathrm{HFE}}(H_{\mathrm{ext}})$ and $\chi''_{\mathrm{HFE}}(H_{\mathrm{ext}})$. The HFE subscripts denote that the field is in the high-field regime and the $\chi'_{\mathrm{HFE}}(H_{\mathrm{ext}})$ and $\chi''_{\mathrm{HFE}}(H_{\mathrm{ext}})$ dependencies correspond to the high-field tail portions of the FMR dispersion and absorption, respectively, according to Eqs. (8) and (9). We see, therefore, that as H_{ext} increases and the susceptibility terms approach zero, the cavity frequency will approach a limiting frequency ω_N and the cavity Q will approach a limiting Q value Q_N. These high-field-limit ω_N and Q_N parameters represent the cavity frequency and cavity Q, respectively, in the limit of no magnetic interactions. As will be evident from Sec. IV, Q_N can contain contributions from eddy current losses in the sample if such losses are significant. The remaining parameter in Eqs. (12) and (13) is the sample/cavity calibration parameter K_{cav}. This parameter can be estimated from cavity perturbation theory[17] or determined empirically. As will be shown below, the high-field effective linewidth analysis procedure yields accurate fitted values for Q_N, ω_N, and K_{cav}, as well as for the high-field effective linewidth ΔH_{HFE}.

A comparison between these perturbation theory connections and the susceptibility equations above yields two relations which may be used to directly determine the high-field effective linewidth. These relations are

$$\omega(H_{\mathrm{ext}})-\omega_N=-K_{\mathrm{cav}}X_F \tag{14}$$

and

$$\frac{1}{Q(H_{\mathrm{ext}})}-\frac{1}{Q_N}=(K_{\mathrm{cav}}\Delta H_{\mathrm{HFE}})X_Q, \tag{15}$$

with X_F and X_Q defined by

$$X_F=\omega\frac{4\pi M_s H_0}{[H_0^2-(\omega/\gamma)^2]} \tag{16}$$

and

$$X_Q=\frac{4\pi M_s[H_0^2+(\omega/\gamma)^2]}{[H_0^2-(\omega/\gamma)^2]^2}. \tag{17}$$

The left-hand sides of Eqs. (14) and (15) show, as before, the explicit dependencies of the cavity frequency ω and cavity Q on H_{ext}. Recall that these two quantities are measured as a function of H_{ext} by the procedure described in Sec. II. From Eqs. (16) and (17) it is clear that X_F and X_Q are also functions of H_{ext} through the variations in the measured frequency ω with field and the connection between the H_0 field parameter and H_{ext} given in Eq. (7). Apart from these variations, X_F and X_Q are completely specified in terms of known parameters. The X_F parameter describes the variation of the FMR magnetic dispersion tail with H_{ext} at high field. The X_Q parameter describes the variation of the FMR magnetic loss tail with H_{ext} at high field.

The high-field effective linewidth analysis is based on the above equations. One starts with an ensemble of cavity

Downloaded 26 Dec 2001 to 129.82.140.114. Redistribution subject to AIP license or copyright, see http://ojps.aip.org/japo/japcr.jsp

frequency ω and cavity Q measurements versus H_{ext}. The first step in the analysis is to evaluate values of the magnetic dispersion tail parameter X_F and the magnetic loss tail parameter X_Q for each (ω,Q,H_{ext}) measurement triplet. The second step in the analysis is to plot ω as a function of X_F. From Eq. (14) such a plot is expected to be linear, have a dimensionless slope m_F equal to $-K_{cav}$, and extrapolate to ω_N at $X_F=0$. Step three, therefore, is to make a straight-line best fit to this plot and thereby obtain empirical determinations of the cavity/sample calibration parameter K_{cav} and the cavity frequency in the high-field limit ω_N. Step four is to make a plot of $1/Q$ as a function of X_Q. From Eq. (15), this plot is also expected to be linear. This linear dependence, however, should yield a slope m_Q equal to $K_{cav}\Delta H_{HFE}$ and an extrapolated value for $1/Q$ at $X_Q=0$ corresponding to $1/Q_N$, the $1/Q$ value in the zero magnetic loss limit. Step five, then, is to make a straight-line best fit to the $1/Q$ vs X_Q data and determine m_Q and $1/Q_N$. The last step in the analysis is to evaluate the value of the ratio $m_Q/|m_F|$. From Eqs. (14) and (15), this ratio is the high-field effective linewidth ΔH_{HFE}.

This method was used on the ensemble of (ω,Q,H_{ext}) data which was obtained as described in Sec. II. Measurements of cavity frequency ω and cavity Q vs static field H_{ext} were made for TE_{011} cylindrical cavities at nominal frequencies of 10.0, 19.3, 35.3, and 60.5 GHz. The data were obtained for a field range of 4–12 kOe for the 10.0, 19.3, and 35.3 GHz frequencies and for a field range of 12–16 kOe at 60.5 GHz. As noted above, the actual FMR peak is inaccessible below 40 GHz for saturated barium ferrite c-plane disks with the external static field along the disk normal. The 4 kOe lower-field limit was selected for the 10, 19, and 35 GHz measurements simply to ensure magnetic saturation. At 60 GHz, the FMR peak is at about 8 kOe and the high-field tail region was examined in the range 12–16 kOe.

The plots of ω vs X_F and $1/Q$ vs X_Q were all quite linear and allowed the determination of the cavity parameters Q_N, ω_N, and K_{cav}, as well as the high-field effective linewidth ΔH_{HFE} for each frequency with high accuracy. A representative plot of ω vs X_F is shown in Fig. 4. This plot is for the same 0.87-mm-thick, 3.0-mm-diam disk and based on the 10 GHz data shown in part in Fig. 3. The evaluation of X_F was based on computed values $N_x=0.16$ and $N_z=0.68$ for the disk demagnetizing factors, along with the experimentally determined values $4\pi M_s=4.73$ kG and $H_A=16.3$ kOe discussed in Sec. II. The plot is quite linear and the absolute value of the fitted slope is given by $|m_F|=(6.71\pm0.01)\times10^{-4}$. This plot derives directly from the cavity frequency versus field data shown in part in Fig. 3. The high degree of linearity and the accurate slope attest to the applicability of the uniform mode model and the high-field approximations embodied in the analysis given above. Moreover, the empirical cavity calibration parameter $K_{cav}=|m_F|$ is reasonably close to the perturbation theory value of 7.3×10^{-4}. As is discussed shortly, the ensemble of fits for different thickness disks and a given cavity give empirical calibration parameters which approach the perturbation theory value in the zero thickness limit. The empirical approach has the advantage, therefore, of allowing for the small changes introduced by the finite sample size and eddy current losses but without sacrificing the simple connection between cavity parameters and resonance response in Eqs. (14) and (15). The fitted frequency intercept at $X_F=0$ in Fig. 4 is $\omega_N=9.969883$ GHz ±2.8 kHz. This frequency corresponds to the resonant frequency of the cavity with the sample in place in the high-field limit of no microwave magnetic response.

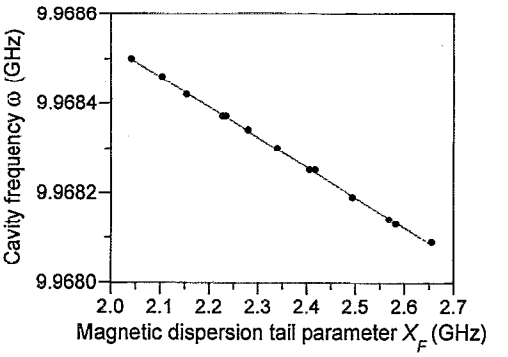

FIG. 4. Plot of cavity frequency ω vs the frequency parameter X_F for a barium ferrite disk of diameter $D=3.0$ mm and thickness $T=0.87$ mm in the center of a 10 GHz TE_{011} cylindrical cavity. The static field was perpendicular to the disk plane and the cavity microwave field was in plane. The solid line represents a straight-line best fit to the data.

A representative plot of $1/Q$ vs X_Q is shown in Fig. 5, also for the same 0.87-mm-thick disk used for the data in Fig. 3. This plot is also quite linear. The fitted slope in this case is $m_Q=(5606\pm50)\times10^{-4}$ Oe. This plot derives directly from the cavity Q versus field data shown in part in Fig. 3. As for the ω vs X_F fit in Fig. 4, the high degree of linearity and the accurate slope attest to the applicability of the uniform mode model and the high-field approximations embodied in the analysis given above. The ratio $m_Q/|m_F|$ gives the high-field effective linewidth. From the values given above, one obtains $\Delta H_{HFE}=(828\pm7)$ Oe. The fitted

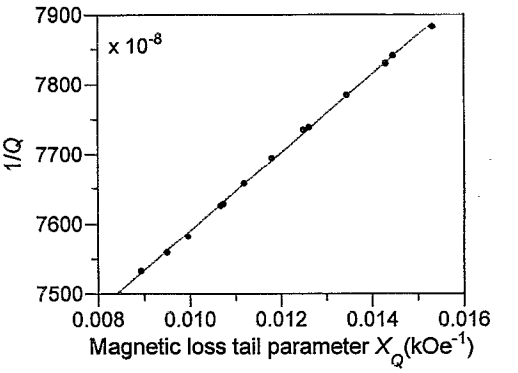

FIG. 5. Plot of $1/Q$ vs the magnetic loss tail parameter X_Q for a barium ferrite disk of diameter $D=3.0$ mm and thickness $T=0.87$ mm in the center of a 10 GHz TE_{011} cylindrical cavity. The static field was perpendicular to the disk plane and the cavity microwave field was in plane. The solid line represents a straight-line best fit to the data.

Downloaded 26 Dec 2001 to 129.82.140.114. Redistribution subject to AIP license or copyright, see http://ojps.aip.org/japo/japcr.jsp

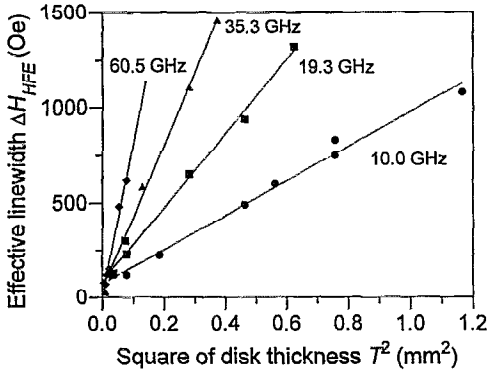

FIG. 6. Plots of effective linewidth ΔH_{HFE} vs the square of the disk thickness T^2 for the four nominal frequencies of measurement, 10, 19, 35, and 60 GHz. The solid lines represent straight-line best fits to the data.

$1/Q$ intercept at $X_Q=0$ in Fig. 5 yields $Q_N=14\,226\pm 13$. This Q_N corresponds to the Q value of the cavity with the sample in place in the limit of no microwave magnetic response.

The results in Figs. 4 and 5 demonstrate the procedure outlined above for the determination of the high-field effective linewidth. The linearity of the plots and the accuracy of the fitted values, especially for ΔH_{HFE}, show the utility of the technique for intrinsic linewidth determinations in ferrites in general. Note that these particular results are for 10 GHz, a frequency below the minimum frequency for ferromagnetic resonance. For barium ferrite at 10 GHz, as pointed out above, FMR occurs for negative fields on the order of -10 kOe. The Q and frequency data in Fig. 3 and the reduced data in Figs. 4 and 5 all correspond to the high-field tail portion of the FMR response. The results show that this tail response, at tens of kOe above FMR, can be used to determine accurate values for microwave magnetic loss parameters such as the high-field effective linewidth ΔH_{HFE} obtained here. A modified tail analysis can also be applied to the data for situations where eddy current losses dominate and the pertinent parameter becomes the microwave conductivity rather than ΔH_{HFE}. These considerations are discussed shortly.

The results of the above analysis applied to frequency and Q data at 10–60 GHz for disks ranging in diameter from 0.5 to 3.2 mm and ranging in thickness from 0.1 to 1.75 mm are shown in Fig. 6 and Table 1. Figure 6 shows values of ΔH_{HFE} as a function of the square of the disk thickness for the four nominal frequencies of measurement. The solid lines show linear fits to the data at each frequency. Ordered by increasing frequency, the fitted slopes are 898, 1944, 3795, and 8070 Oe/mm^2, respectively. The value of the effective linewidth extrapolated to zero thickness for each frequency is less than 100 Oe. The data for 10 GHz are the same as Ref. 8. The new data for the higher frequencies show that ΔH_{HFE} increases with the square of the sample thickness at these frequencies as well. These data also show that the slope of the response scales linearly with frequency. Both responses indicate that the predominant source of the linewidth is eddy current losses. The connection between the above numerical values for the fitted slopes and microwave conductivity is more complicated than indicated by Eq. (9) in Ref. 8. This connection is discussed in the Appendix.

TABLE I. Summary of disk samples and high-field effective linewidth results.

f (GHz)	T (mm)	D (mm)	ΔH_{HFE} (Oe)	$K^e_{\mathrm{cav}}/K^p_{\mathrm{cav}}$
10.0	0.28	3.1	120	1.02
	0.43	3.0	225	0.97
	0.68	2.9	490	0.99
	0.75	3.2	600	1.04
	0.87	3.2	750	1.00
	0.87	3.0	830	1.08
	1.08	3.2	1080	1.10
	1.23	3.2	1350	1.10
	1.35	3.2	1650	1.16
	1.40	3.2	1850	1.16
	1.75	3.2	2900	1.22
19.3	0.18	2.0	123	0.90
	0.19	3.0	126	0.90
	0.28	2.0	230	0.92
	0.53	1.3	650	1.03
	0.65	1.3	940	1.10
	0.79	2.9	1320	1.32
35.3	0.14	1.2	130	1.00
	0.15	1.3	145	1.00
	0.36	1.4	300	1.13
	0.53	1.3	900	1.30
	0.61	1.0	1450	1.49
60.5	0.10	0.5	70	...
	0.12	0.5	120	...
	0.15	0.5	150	...
	0.23	0.5	480	...
	0.28	0.5	620	...

Table I lists the specific samples for the measurements at 10.0, 19.3, 35.3, and 60.5 GHz, along with the actual values of ΔH_{HFE} for each sample/frequency combination. The column label T denotes disk thickness. The column label D denotes disk diameter. Within each frequency grouping, the disk sizes are listed in order of increasing sample volume. The last column in Table I lists values of the $K^e_{\mathrm{cav}}/K^p_{\mathrm{cav}}$ ratios for the empirically determined cavity calibration parameter K^e_{cav} and the K^p_{cav} value from perturbation theory for each sample. It is noteworthy that these ratios approach unity for the smaller samples, the limit in which one would expect perturbation theory to be most accurate. It is also noteworthy that the departures in K^e_{cav} from the perturbation theory value are significant for the larger samples and are typically on the order of 10%–20%. This is true even when the actual data involve relatively small changes in cavity Q and frequency from the high-field-limit values, ω_N and Q_N. It is clear that accurate effective linewidth determinations require use of the empirical calibration procedure. Reliance on perturbation theory formulas can lead to significant errors.

In spite of the consistency and good agreement with theory described above, it is hard to argue that the ΔH_{HFE} linewidth parameters presented in Fig. 6 and Table I are

Downloaded 26 Dec 2001 to 129.82.140.114. Redistribution subject to AIP license or copyright, see http://ojps.aip.org/japo/japcr.jsp

really "intrinsic." One does not expect an "intrinsic" linewidth to change with sample dimension. While eddy currents may be "intrinsic" to the microwave response in these moderate conductivity barium ferrite materials, a linewidth parameter which changes with sample thickness is clearly not intrinsic. It is well established that the high-field effective linewidth procedure gives *bona fide* intrinsic linewidth values when the mechanisms themselves are intrinsic, as for dense, high-purity yttrium iron garnet (YIG)[3] or rare-earth-substituted YIG.[18]

A somewhat better approach when eddy current losses are important would be to model these losses separately from the contributions due to the magnetic losses. Such modeling would allow one to use the same basic measurements described above and then make modified fits to those measurements to determine the microwave or millimeter wave conductivity of the sample. Such eddy current modeling for barium ferrite is summarized in Sec. IV, along with the requisite changes in the plotting and fitting procedure to determine the microwave conductivity from the resonance high-field tail data.

IV. EDDY CURRENT LOSS ANALYSIS

The high-field far-from-resonance eddy current losses at microwave frequencies in barium ferrite disks can be analyzed on the basis of a simple model. First, as in Sec. III, the external microwave magnetic field excites a uniform mode magnetic response in the disks as given by Eqs. (2) and (7)–(11). Second, these time-dependent contributions to the magnetic induction $\mathbf{b}(t)=\mathbf{h}(t)+4\pi\mathbf{m}(t)$ give rise to a microwave electric field of the form $\mathbf{e}(z,t)$ which generates eddy currents and leads to additional loss. This z-dependent electric field is specific to the present thin slab geometry. The average eddy current loss of the disk sample is obtained by a simple integration over the disk thickness. Just as the magnetic loss due to the response $\mathbf{m}(t)$ corresponds to the high-field tail of the FMR absorption and dispersion curves discussed in Sec. III, the eddy current losses driven by this response also contribute to the overall FMR absorption curve high-field tail response observed experimentally. The final step in this eddy current loss analysis is to develop connections between the high-field eddy current tail (ECT) response by means of an eddy current tail parameter X_C and change in cavity Q, in the format of Eqs. (13) and (15). As indicated above, these connections allow one to make linear plots of $1/Q$ versus this new X_C parameter and extract the microwave conductivity σ from the slopes of such plots, in much the same way that $1/Q$ vs X_Q plots yielded values of ΔH_{HFE} in Sec. III. The high-field limit $1/Q$ values from the $1/Q$ vs X_C plot intercepts, $1/Q_\sigma$, counterparts to the $1/Q_N$ parameter in Sec. III, now have an explicit eddy current loss contribution as well. Analysis of the variation of these $1/Q_\sigma$ values versus disk thickness provides an additional way to determine the microwave conductivity.

It is important to emphasize that this simple model is valid only in the far-from-resonance limit. In this limit, where the magnetic response driving the eddy currents is small, the eddy currents are small, and the magnetic fields generated by the eddy currents do not appreciably modify the magnetic response. Closer to resonance or for materials with higher conductivity, a full self-consistent solution of the magnetic response and the Maxwell equations with appropriate boundary conditions is necessary. Such solutions are well established for a variety of FMR and related phenomena.[19] The present approach, however, is much simpler, more intuitive, and amenable to simple analysis.

Consider the total dissipated power in the barium ferrite disk. The total power loss P may be written as the sum of two terms,

$$P=P_{\mathrm{mag}}+P_{\mathrm{ec}}, \tag{18}$$

where P_{mag} is the loss associated with magnetic loss processes and P_{ec} represents the ohmic losses associated with the induced eddy currents and the nonzero resistivity of the material. For the geometry under consideration here, the magnetic loss is connected to the $4\pi\chi''_{\mathrm{mag}}$ term in the magnetic response presented in Sec. III through the well known expression[20]

$$P_{\mathrm{mag}}=V(\omega h^2/8\pi)(4\pi\chi''_{\mathrm{mag}}), \tag{19}$$

where V is the sample volume and h is the amplitude of the linearly polarized external microwave field. Recall that $4\pi\chi''_{\mathrm{mag}}$ also enters explicitly into the effect of magnetic loss on cavity Q, through Eq. (13) in Sec. III. Equations (13) and (19), therefore, provide a direct connection between the change in cavity Q and any power loss which scales with the square of the microwave magnetic-field amplitude and the sample volume. As will be evident from the development given below, P_{ec} also scales with the square of the microwave-field amplitude and the sample volume. These dependencies make possible the definition of an X_C parameter and the extraction of the microwave conductivity σ from plots of $1/Q$ vs X_C in much the same way that plots of $1/Q$ vs X_Q were used in Sec. III to extract a high-field effective linewidth. The details of the analysis are given below.

Figure 7 shows a schematic representation of a disk sample of thickness T and the magnetization-field geometry for the eddy current tail response analysis. The x-y-z coordinate system and sample setup are the same as in Sec. III. The disk is positioned with the center plane at $z=0$ and the disk surfaces at $z=\pm T/2$. The disk is magnetized to saturation in the perpendicular z direction by the static magnetic field H_{ext}. The saturation magnetization M_s is parallel to H_{ext}. The external microwave field $\mathbf{h}$ is now taken to be parallel to the y axis and is denoted by h_y in the figure. The dynamic transverse x-y dynamic magnetization $\mathbf{m}(t)$ is denoted by the $\mathbf{m}$ vector and x-y plane precession circle. The x and y components of the induced electric field $\mathbf{e}(z,t)$ are shown by the arrows labeled e_x and e_y. It is assumed that z-directed currents are suppressed by the thin slab geometry; z-component electric fields and currents are neglected. Even though the disk is shown in Fig. 7 with a definite diameter, the analysis is based on a disk of infinite extent.

With the dynamic magnetization response $\mathbf{m}(t)$ as given in Sec. III and the magnetic induction $\mathbf{b}(t)$ given by

Downloaded 26 Dec 2001 to 129.82.140.114. Redistribution subject to AIP license or copyright, see http://ojps.aip.org/japo/japcr.jsp

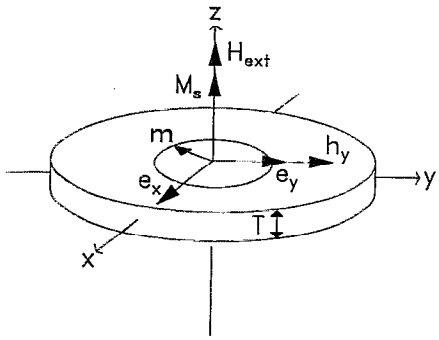

FIG. 7. Schematic diagram of the sample geometry and fields for the FMR eddy current tail analysis for c-plane barium ferrite disks. The disk, of thickness T, is centered in the x-y plane with the static external magnetic field H_{ext} and the magnetic induction M_s along the z axis. The external microwave field h_y is along the y axis. The vector $\mathbf{m}$ denotes the in-plane ferromagnetic resonance (FMR) microwave magnetization vector and the circle denotes the FMR precession cone. The induced in-plane electric-field components are denoted by e_x and e_y. .

$\mathbf{b}(t)=\mathbf{h}(t)+4\pi\mathbf{m}(t)$, the x and y components of the induced electric field $\mathbf{e}(t)$ are readily obtained from the Maxwell equation

$$\nabla\times\mathbf{e}(\mathbf{r},t)=(-i\omega/c)\mathbf{b}(t), \tag{20}$$

where $\mathbf{e}(\mathbf{r},t)=\mathbf{e}(\mathbf{r})e^{i\omega t}$ denotes the complex time- and space-dependent electric field generated by the spatially uniform but time-dependent magnetic induction $\mathbf{b}(t)$. Equation (20) and all equations that follow assume an $e^{i\omega t}$ time dependence for all dynamic fields, as in Sec. III. For the geometry of Fig. 7, one obtains complex electric field amplitude components given by

$$e_x(z)=(-i\omega z/c)(4\pi m_y+h_y) \tag{21}$$

and

$$e_y(z)=(i\omega z/c)4\pi m_x. \tag{22}$$

The electric field from Eqs. (21) and (22) generates an associated current-density distribution $\mathbf{j}(z,t)$ according to Ohm's law, $\mathbf{j}=\sigma\mathbf{e}$, where σ denotes the conductivity. Note that the electric fields and the current density is zero at the midplane of the disk and increases linearly with z to positive and negative maxima at the disk surfaces. This current leads to a time-averaged power dissipation for the entire disk which varies as the cube of the disk thickness T. The time averaged power dissipation per unit volume then scales as the square of the disk thickness. This is the origin of the quadratic scaling of the eddy current based effective linewidth with disk thickness observed in Sec. III.

The time-averaged power dissipation P_{ec} for a disk of thickness T and surface area A is given by

$$P_{ec}=\frac{A}{2}\int_{-T/2}^{T/2}\sigma|\mathbf{e}(z)|^2\,dz$$

$$=\frac{\sigma AT^3\omega^2}{24c^2}(|4\pi m_y|^2+2|4\pi m_y h_y|+|h_y|^2+|4\pi m_x|^2). \tag{23}$$

Note again that P_{ec} is the power loss for the entire disk of volume $V=AT$. The power dissipation per unit volume P_{ec}/AT scales with the square of the disk thickness T. The eddy current losses also scale with the microwave conductivity σ.

The quadratic dependence of P_{ec} on the microwave field amplitude h_y is also evident from Eq. (23). From the magnetic response equations in Sec. III, m_x and m_y scale linearly with h_y according to

$$m_x=-i\kappa_{mag}h_y \tag{24}$$

and

$$m_y=\chi_{mag}h_y. \tag{25}$$

These dependencies give a P_{ec} that varies as the square of the microwave field amplitude and may be written in the same format as Eq. (19),

$$P_{ec}=(AT)(\omega h_y^2/8\pi)(4\pi\chi_{ec}+4\pi\chi_{bg}), \tag{26}$$

with $4\pi\chi_{ec}$ and $4\pi\chi_{bg}$ given by

$$4\pi\chi_{ec}=\frac{\pi\omega\sigma T^2}{3c^2}(|4\pi\chi_{mag}|^2+2|4\pi\chi_{mag}|+|4\pi\kappa_{mag}|^2) \tag{27}$$

and

$$4\pi\chi_{bg}=\pi\omega\sigma T^2/3c^2. \tag{28}$$

Several points are to be noted with regard to Eqs. (26), (27), and (28). First, the volume factor in Eq. (19) is factored out as AT in Eq. (26). This makes explicit the T^2 dependence for $4\pi\chi_{ec}$ and $4\pi\chi_{bg}$. Second, $4\pi\chi_{ec}$ and $4\pi\chi_{bg}$ are not actual "susceptibility" components. They are simply variables which play the same role as the magnetic susceptibility loss component in the power loss formulas for eddy currents. Third, the additional nonresonant $4\pi\chi_{bg}$ term in Eq. (26), not present in Eq. (19), is due to the background eddy current losses from the currents induced by h_y alone in the $|h_y|^2$ term in Eq. (23). As shown below, this background eddy current loss does not contribute to the FMR eddy current tail response and becomes part of the nonmagnetic cavity losses embedded in the high-field-limit Q value.

As evident by the square bracket term in Eq. (27), the eddy current losses are driven by all of the χ and κ terms in the magnetic response, not just χ''_{mag}. In the far-from-resonance high-field eddy current tail regime of interest here, the combination of χ and κ terms in the square bracket term simplifies considerably, just as the χ_{mag} and κ_{mag} expressions simplified to the χ_{HFE} and κ_{HFE} expressions in Sec. III. In this case, the surviving terms involve only the expressions for $4\pi\chi'_{HFE}$ and $4\pi\kappa'_{HFE}$ in Eqs. (8) and (10). This eddy current tail ECT regime is the same as the HFE regime in Sec. III. In this regime, one may write $4\pi\chi_{ec}$ in Eq. (27) as

$$4\pi\chi_{ECT}=4\pi M_s\frac{\pi\omega\sigma T^2}{3c^2}\left(\frac{2H_0}{[H_0^2-(\omega/\gamma)^2]}+X_Q\right). \tag{29}$$

The X_Q parameter is the same as in Eq. (17) from Sec. III.

Downloaded 26 Dec 2001 to 129.82.140.114. Redistribution subject to AIP license or copyright, see http://ojps.aip.org/japo/japcr.jsp

The ECT eddy current tail analysis is nearly complete. One now writes an equation in the format of Eq. (15) but for the eddy current tail response rather than the magnetic losses. The right-hand side of the equation derives from Eq. (13) but with $\chi''_{\rm mag}$ replaced by $\chi_{\rm ECT}$ from Eq. (29). The $1/Q_N$ term on the left-hand side must be replaced by a $1/Q_\sigma$ parameter which includes the contribution of the nonresonant background eddy current losses in the sample to the cavity Q at infinite field. The result is

$$[1/Q(H_{\rm ext})]-(1/Q_\sigma)=(K_{\rm cav}G_{\rm ECT})X_C. \tag{30}$$

The $G_{\rm ECT}$, X_C, and Q_σ parameters are given by

$$G_{\rm ECT}=4\pi M_s(2\pi\omega\sigma T^2/3c^2), \tag{31}$$

$$X_C=\frac{2H_0}{[H_0^2-(\omega/\gamma)^2]}+X_Q, \tag{32}$$

and

$$\frac{1}{Q_\sigma}=\frac{1}{Q_{\rm emp}}+\frac{K_{\rm cav}G_{\rm ECT}}{4\pi M_s}. \tag{33}$$

The $G_{\rm ECT}$ parameter in Eq. (30) plays the same role in the $1/Q$ vs X_C fitting procedure as does $\Delta H_{\rm HFE}$ in the $1/Q$ vs X_Q fitting procedure. Note that $G_{\rm ECT}$ has units of Gauss and that the square bracket term in Eq. (31) is dimensionless. Conductivity in cgs units has dimensions of s^{-1}. The eddy current tail parameter X_C is given explicitly in Eq. (32). This parameter describes the eddy current FMR absorption tail response in the same way that the magnetic loss tail parameter X_Q in Eq. (17) describes the magnetic loss FMR absorption tail. The connection between plots of $1/Q$ vs X_C and the plots of $1/Q$ vs X_Q in Sec. III is discussed at the end of this section and in the Appendix.

The high-field limit $1/Q$ parameter is now given by $1/Q_\sigma$. As given in Eq. (33), $1/Q_\sigma$ contains two terms. The $Q_{\rm emp}$ term relates to the losses for the bare cavity. The second term in Eq. (33) relates to the eddy current losses due to the induced currents in the sample by the applied microwave field. The connection between $1/Q_\sigma$ and the $1/Q_N$ parameter of Sec. III is discussed in the Appendix.

In general, Eq. (30) would also contain an additive $(K_{\rm cav}\Delta H_{\rm HFE})X_Q$ term from Eq. (15), but with $\Delta H_{\rm HFE}$ now taken as the intrinsic linewidth for magnetic losses alone. For the barium ferrite materials of interest here, however, the magnetic loss contribution to the tail response is quite small compared to the eddy current contribution. This conclusion is clear from Fig. 6. The vertical axis intercepts for straight line fits for the $\Delta H_{\rm HFE}$ vs T^2 plots in Fig. 6 are all below 100 Oe. These intercepts correspond to the intrinsic part of the $\Delta H_{\rm HFE}$ parameter. The eddy current loss part of the $\Delta H_{\rm HFE}$ data in Fig. 6 is the part which increases with T^2. Figure 6 shows, therefore, that the FMR tail response is almost entirely due to the eddy current losses. The neglect of the magnetic loss term in Eq. (30) is quite reasonable in the present context.

The ECT plotting and fitting procedure is similar to the HFE linewidth procedure: (i) One first makes a plot of $1/Q$ vs X_C in place of the $1/Q$ vs X_Q plot of Sec. III and does a linear best fit; (ii) one uses the fitted slope, taken as

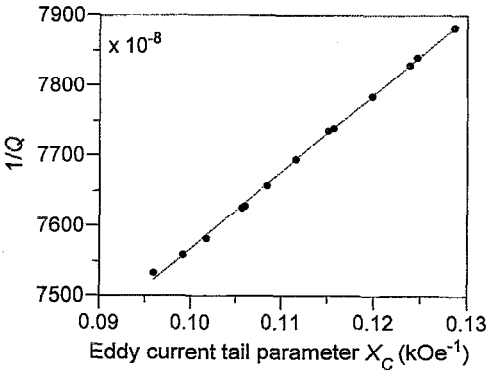

FIG. 8. Plot of $1/Q$ vs the eddy current tail parameter X_C for a barium ferrite disk of diameter $D=3.0$ mm and thickness $T=0.87$ mm in the center of a 10 GHz TE_{011} cylindrical cavity. The static field was perpendicular to the disk plane and the cavity microwave field was in plane. The solid line represents a straight-line best fit to the data.

$K_{\rm cav}G_{\rm ECT}$, along with the fitted slope from the companion ω vs X_F plot described in Sec. III, taken as $-K_{\rm cav}$, to determine $G_{\rm ECT}$; (iii) one then uses Eq. (31), along with the known values for the saturation induction $4\pi M_s$, frequency ω, and disk thickness T, and evaluates the microwave conductivity σ. Figure 8 shows a representative plot of $1/Q$ vs X_C, based on the same 10 GHz data used for the example plots in Sec. III. The plot is quite linear. The slope of the straight-line best fit shown in the figure is equal to (0.1095 ± 0.0011) G. Taking this slope as $K_{\rm cav}G_{\rm ECT}$ from Eq. (30) and using $K_{\rm cav}=(6.71\pm0.01)\times10^{-4}$ from the ω vs X_F plot for the same data in Sec. III, one obtains a value of (163 ± 2) G for $G_{\rm ECT}$. The microwave conductivity σ can be obtained directly from $G_{\rm ECT}$. The conductivity obtained from the ECT response analysis described above for a single sample is denoted as $\sigma_{\rm ECT}$. Expressed in practical units, $\sigma_{\rm ECT}$ in units of $\Omega^{-1}\,{\rm cm}^{-1}$ is related to $G_{\rm ECT}$, the frequency ω, the saturation induction $4\pi M_s$, and the disk thickness T according to

$$\sigma_{\rm ECT}\ (\Omega^{-1}\,{\rm cm}^{-1})=\frac{3G_{\rm ECT}\ ({\rm G})}{(2\pi)^2\omega\ ({\rm GHz})[T\ ({\rm cm})]^2 4\pi M_s\ ({\rm G})}. \tag{34}$$

The conductivity from the 10 GHz results presented above for the $T=0.87$ mm disk is obtained as $\sigma_{\rm ECT}=(0.0347\pm0.0003)\ \Omega^{-1}\,{\rm cm}^{-1}$.

We turn now to the vertical intercept of the straight-line fit to the data in Fig. 8. This intercept corresponds to the $1/Q_\sigma$ parameter in Eq. (30). The straight line fit in Fig. 8 yields $1/Q_\sigma=(6.473\pm0.005)\times10^{-5}$. Determinations of $1/Q_\sigma$ in this manner for a given frequency and disks of different thicknesses provide a second determination of the microwave conductivity. Equations (31) and (33) indicate that $1/Q_\sigma$ should vary linearly with the parameter combination $K_{\rm cav}T^2$. Recall that $K_{\rm cav}$ varies with the disk thickness. The linear variation should have a slope equal to $2\pi\omega\sigma/3c^2$ and extrapolate to the bare cavity $1/Q$ value $1/Q_{\rm emp}$, in the $T=0$ limit. Figure 9 shows such a plot of

Downloaded 26 Dec 2001 to 129.82.140.114. Redistribution subject to AIP license or copyright, see http://ojps.aip.org/japo/japcr.jsp

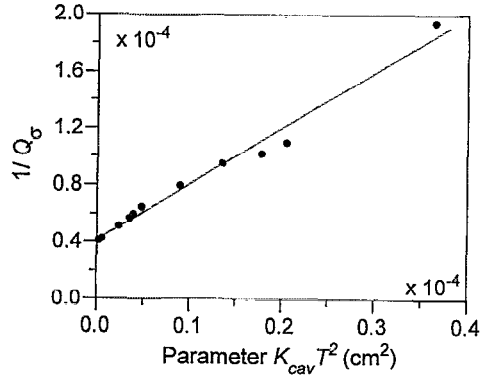

FIG. 9. Plot of the fitted $1/Q_\sigma$ parameter vs the parameter combination $K_{cav}(T)T^2$, for the 10 GHz samples and cavity. The solid line represents a straight-line best fit to the data.

$1/Q_\sigma$ vs $K_{cav}T^2$ obtained from the 10 GHz data for the 11 disks listed in Table I. The straight-line fit to the data has a slope $m_\sigma = (3.9 \pm 0.2)$ cm^{-2}. This slope parameter converts to microwave conductivity according to

$$\sigma_Q\ (\Omega^{-1}\,\mathrm{cm}^{-1}) = 3m_\sigma\ (\mathrm{cm}^{-2})/(2\pi)^2\omega\ (\mathrm{GHz}). \tag{35}$$

The value of σ_Q from the 10 GHz fit in Fig. 9 is $(0.030 \pm 0.002)\ \Omega^{-1}\,\mathrm{cm}^{-1}$. This all-sample value is in good agreement with the $T = 0.87$ mm single sample σ_{ECT} value obtained above. The vertical axis intercept of the straight-line fit in Fig. 9 also yields a value for the bare cavity Q, Q_{emp}. The intercept in Fig. 9 yields $Q_{emp} = 24\,300 \pm 2000$. This value of Q_{emp} is in good agreement with the measured Q for the 10 GHz cavity with no sample, $24\,500 \pm 1000$.

The results of the data analyses and fits to obtain σ_{ECT} and σ_Q at the four nominal frequencies of measurement, 10, 19, 35, and 60 GHz, for all the samples are shown in Fig. 10. The σ_{ECT} points in Fig. 10 represent average values for all the samples for a given frequency. The value of the dc conductivity σ_{dc} shown by the point at zero frequency

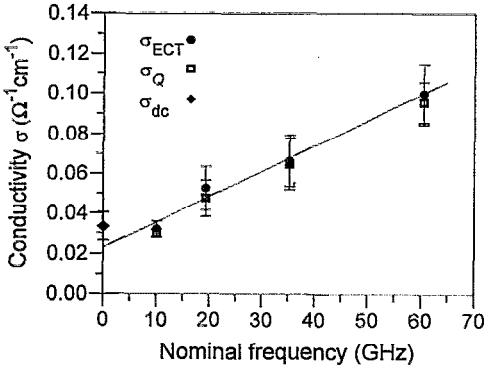

FIG. 10. Plot of microwave conductivity vs frequency for the four nominal frequencies of measurement. The solid circles show the averaged values for the σ_{ECT} determinations on the individual disks at each frequency. The open squares show the σ_Q values obtained for each frequency. The solid line represents a straight-line best fit to the σ_{ECT} results. The solid diamond shows the measured dc conductivity.

was measured by a standard four-point probe method for a 3-mm-diam 0.5-mm-thick disk sample. The microwave conductivity is seen to increase from about 0.033 $\Omega^{-1}\,\mathrm{cm}^{-1}$ at 10 GHz to 0.10 $\Omega^{-1}\,\mathrm{cm}^{-1}$ at 60 GHz. The slope of the straight line fit in Fig. 10 is (0.0013 ± 0.0001) $\Omega^{-1}\,\mathrm{cm}^{-1}\,\mathrm{GHz}^{-1}$. Figure 10 shows that the σ_{ECT} values from the individual sample eddy current tail analyses and the σ_Q values from the $1/Q_\sigma$ vs $K_{cav}T^2$ fits for all samples at a given frequency are consistent and in good agreement. The overall results in Fig. 10 indicate that the microwave conductivity in M-type barium ferrite increases linearly with increasing frequency.

The source of the moderate conductivity in barium ferrite is attributed to electron hopping between Fe ions due to the presence of Fe^{2+} in the crystal.[13,21] This process gives rise to the conductivity in the crystal as a result of electron hopping between equivalent lattice sites containing Fe^{2+} and Fe^{3+} ions with a characteristic hopping time T_{hop}. This hopping process contributes both to the conductivity and to the magnetic relaxation. The effect of Fe^{2+}-Fe^{3+} electron hopping, sometimes termed "valence exchange," on microwave relaxation and electrical conduction is discussed extensively in the literature. The key reference on Fe^{2+}-Fe^{3+} microwave relaxation is Sparks.[22] Key references on electrical conductivity in ferrites are Smit and Wijn[23] and Parker.[24] By analogy with polaron theory, Parker argues that in the limit of a high hopping probability relative to the tunneling probability for electrons between neighboring ions, one would expect a frequency dependence for the conductivity of the form

$$\sigma(\omega) \propto \omega T_{hop}/[1+(\omega T_{hop})^2]. \tag{36}$$

It is clear from results on magnetic relaxation[22] that the condition $\omega T_{hop} \ll 1$ is well satisfied for microwave frequencies and room temperature. In this limit, the conductivity $\sigma(\omega)$ in Eq. (36) increases linearly with frequency ω. In a more general context, Jonscher[25] has also argued for a conductivity which is a linear function of frequency due to hopping processes for a wide variety of nonmagnetic materials.

In closing this section it is useful to comment on (i) possible dielectric loading effects and (ii) the connections between the eddy current tail analysis presented above and the effective linewidth analysis of Sec. III.

The eddy current analysis given above considers only the effect of the electric field produced through the time-dependent magnetic induction $\mathbf{b}(t)$ at the sample position, as given in Eqs. (20)–(22). Even though the sample is placed at a position in the microwave cavity where the electric field for the TE_{011} cavity mode is nominally zero, the cavity electric field is not exactly zero over the entire volume of the finite size sample. Due to the large conductivity, moreover, the dielectric loss tangent for these materials is large, typically on the order of 0.1–1 in the 100–10 GHz range of frequencies. It is possible, therefore, that some part of the nonmagnetic losses are dielectric losses. However, if these dielectric losses were significant, the σ_{ECT} values obtained from the magnetic response tail analysis for individual samples at a given frequency would be

Downloaded 26 Dec 2001 to 129.82.140.114. Redistribution subject to AIP license or copyright, see http://ojps.aip.org/japo/japcr.jsp

lower than the σ_Q values determined from the change in the high-field limit $1/Q_\sigma$ with $K_{cav}T^2$. The fact that the σ_{ECT} and σ_Q results are virtually identical indicates that dielectric loading is not significant.

We turn now to the ECT/HFE connection. Based on the results given above, it is now clear that the correct analysis is in terms of eddy current losses, the eddy current tail parameter X_C, and the microwave conductivity. This conclusion, however, means that the original interpretation of the slope and intercept parameters from the $1/Q$ vs X_Q plots of Sec. III needs revision. The slope must be related to conductivity and disk thickness in a manner consistent with the eddy current results. The $1/Q$ intercept value $1/Q_N$ must also contain a sample eddy current component.

The Appendix presents a reexamination of the HFE analysis, based on an actual tail response which has its physical origin in eddy current losses. The Appendix establishes connections between the conventional high-field effective linewidth analysis in Ref. 8 and Sec. III and the eddy current tail analysis presented above. The basic conclusion is that for the present samples, frequencies, and field ranges, $1/Q$ versus the HFE X_Q tail parameter is approximately linear and the two approaches are consistent. This is not the case of other materials and other frequency/field regimes.[26] Situations in which the magnetic losses and eddy current losses are comparable would require a more extensive analysis of a hybrid tail response.

V. SUMMARY AND CONCLUSION

The losses associated with the high-field tail region of the ferromagnetic resonance (FMR) absorption curve were investigated at 10, 19, 35, and 60 GHz for 0.10–1.75-mm-thick *c*-plane circular disks of flux-grown single-crystal M-type barium ferrite with the static field perpendicular to the disk plane. Microwave and millimeter wave cavity Q and cavity frequency measurements were made for fields from well above the FMR field position up to 16 kOe.

A conventional high-field magnetic loss analysis of the data in terms of an effective linewidth ΔH_{HFE} yielded values of ΔH_{HFE} which increase with the square of the disk thickness and linearly with frequency. These dependencies indicate that the predominant source of the linewidth in these disk samples is eddy current losses.

Based on these results, an eddy current loss analysis of the tail region was done, based on the insulator FMR response and eddy current losses driven by the FMR response. The conductivity is obtained from an appropriate analysis of the FMR absorption tail, just as the effective linewidth analysis of the high-field FMR tail yields a high-field effective linewidth parameter. Based on this technique, the microwave conductivity of these flux-grown barium ferrite single-crystal materials was determined as a function of frequency from 10 to 60 GHz. The microwave conductivity increases linearly with frequency, from $0.033 \pm 0.004\ \Omega^{-1}\,cm^{-1}$ at 10 GHz to $0.10 \pm 0.02\ \Omega^{-1}\,cm^{-1}$ at 60 GHz. These results are consistent with a measured dc resistivity of 0.03–0.05 $\Omega^{-1}\,cm^{-1}$.

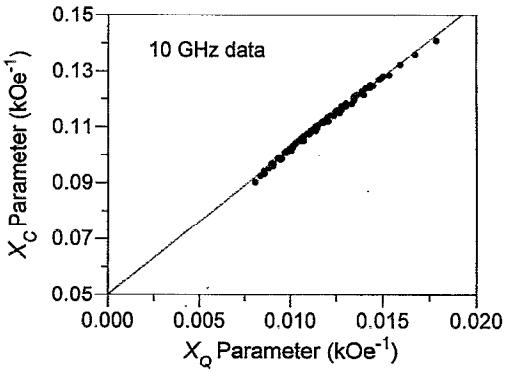

FIG. 11. Plot of the magnetic loss tail parameter X_Q vs the eddy current tail parameter X_C for the 4–12 kOe high-field FMR tail range applicable to the 10 GHz data HFE and ECT analyses.

ACKNOWLEDGMENTS

This work was supported in part by the United States Office of Naval Research, Grant No. N00014-90-J-4078 and the United States Army Research Office, Grant No. DAAL03-91-G-0327. The barium ferrite single-crystal materials were kindly provided by Dr. M. A. Wittenauer of Purdue University. Professor S. Shtrikman, Weitzmann Institute of Science, and Professor F. J. Friedlaender, Purdue University, initially suggested the possibility of eddy current losses as a linewidth source in pure barium ferrite. The hard direction hysteresis curve extrapolation procedure to determine anisotropy fields was suggested by Professor J. Nyenhuis of Purdue University. Professor C. Vittoria, Northeastern University, is gratefully acknowledged for helpful advice on the shaping of disk samples for microwave and millimeter wave measurement.

APPENDIX

The objective of this appendix is to reexamine the Sec. III results in light of the new eddy current tail analysis and results of Sec. IV. The starting point for this reexamination is with the $X_Q(H_{ext})$ and the $X_C(H_{ext})$ functions which represent the magnetic and eddy current FMR tail responses for the high-field regimes of interest here. As Eqs. (7), (17), and (32) indicate, $X_Q(H_{ext})$ and $X_C(H_{ext})$ are not, in general, connected in a linear fashion. This would further indicate that if plots of $1/Q$ vs X_C are linear, then plots of $1/Q$ vs X_Q should, in general, not be linear and a simple interpretation of the data in terms of a single high-field effective linewidth parameter should not be possible. This is, in fact, the situation for moderate conductivity planar hexagonal ferrite materials.[26] In the case of barium ferrite disks and the extreme high-field tail regimes examined here, however, the X_Q and X_C functions are, to a good approximation, linearly related.

Figure 11 shows a representative plot of X_C vs X_Q which includes all the data points for all the samples used for the 10 GHz results in Secs. III and IV. Keep in mind that the connection between X_C and X_Q is not simply through Eqs. (7), (17), and (32) for a given change in

Downloaded 26 Dec 2001 to 129.82.140.114. Redistribution subject to AIP license or copyright, see http://ojps.aip.org/japo/japcr.jsp

H_{ext} with other parameters fixed. The actual data reflect changes in the frequency ω with H_{ext} and different values of the N_x and N_z demagnetizing factors for the different 10 GHz samples. The data connection in Fig. 11 between X_C and X_Q is reasonably linear. The straight-line best fit shown in the figure has a slope $S(10,H)=5.19\pm0.03$ and an intercept $I(10/H)=0.0503\pm0.0007$ kOe^{-1}. The $(10,H)$ notation is intended to indicate that these particular numbers (i) apply to the 10 GHz data and (ii) depend on the range of magnetic fields for which the data were taken. S and I are strictly operational- and experiment-dependent parameters which will change with the nominal frequency f and the high-field tail regime selected for measurement. For a given frequency band, this operational connection between X_C and X_Q may be written as

$$X_C=S(f,H)X_Q+I(f,H), \tag{A1}$$

where $S(f,H)$ and $I(f,H)$ denote the frequency band f and field-range-dependent H operational slope S and intercept I parameters from plots of X_C vs X_Q for the 10, 19, 35, and 60 GHz data. From Eq. (A1), Eq. (30) may now be cast into a form compatible with Eq. (15) in Sec. III. One obtains expressions for the Eq. (15) slope parameter ΔH_{HFE} and intercept parameter $1/Q_N$ in terms of parameters from the ECT analysis:

$$\Delta H_{HFE}=G_{ECT}S(f,H)=4\pi M_s\left(\frac{2\pi\omega\sigma T^2}{3c^2}\right)S(f,H). \tag{A2}$$

$$\frac{1}{Q_N}=\frac{1}{Q_{emp}}+K_{cav}(T)G_{ECT}\left(\frac{1}{4\pi M_s}+I(f,H)\right)$$
$$=\frac{1}{Q_{emp}}+K_{cav}(T)\left(\frac{2\pi\omega\sigma T^2}{3c^2}\right)[1+4\pi M_s I(f,H)]. \tag{A3}$$

Equations (A2) and (A3) make explicit connections between the results of the ECT analysis and the HFE analysis of Sec. III. Recall from Eq. (31) that G_{ECT} varies linearly with the conductivity σ and the square of the disk thickness T. The second lines of Eqs. (A2) and (A3) incorporate the explicit form of G_{ECT} from Eq. (31). The K_{cav} cavity calibration parameter in Eqs. (A2) and (A3) is written as $K_{cav}(T)$ to make the sample size dependence explicit. The basic result from Sec. III, a ΔH_{HFE} parameter which increases with the square of the disk thickness T, is evident from Eq. (A2). Equation (A2) also shows that this ΔH_{HFE} parameter depends on the frequency- and field-range-dependent parameter $S(f,H)$. The important conclusion here is that ΔH_{HFE} is not a physically meaningful parameter for moderate conductivity ferrites. Any interpretation of experimental data in terms of an effective linewidth must be made with a full understanding of the ECT procedure embodied in Eq. (A2).

Turn now to the $1/Q_N$ intercept parameter in Eq. (A3). Equation (A3) indicates that the $1/Q_N$ parameter for the different samples measured at a given nominal frequency should scale linearly with the quantity $K_{cav}(T)T^2$, with an intercept equal to $1/Q_{emp}$ and a slope related to the conductivity σ. This slope, however, also depends on the intercept parameter $I(f,H)$. Figure 12 shows a plot of $1/Q_N$ versus the quantity $K_{cav}(T)T^2$ from the 10 GHz data. The straight-line best fit to the data, shown by the solid line, has an intercept corresponding to $Q_{emp}=23\,600\pm1000$ and a slope corresponding to a conductivity $\sigma=(0.0305\pm0.0015)\ \Omega^{-1}\,\mathrm{cm}^{-1}$. Both values are consistent with the results presented in Sec. IV.

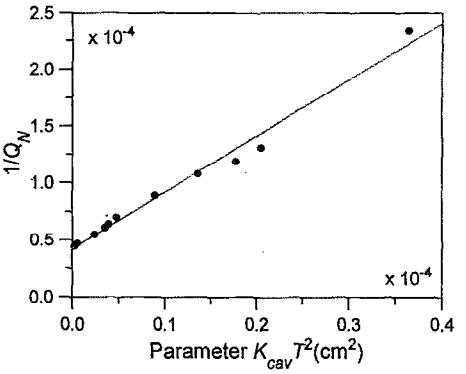

FIG. 12. Plot of the 10 GHz fitted $1/Q_N$ values vs the parameter combination $K_{cav}(T)T^2$ for the 10 GHz samples and cavity. The solid line represents a straight-line best fit to the data.

Finally, we turn now to the connection between Eq. (A2) and the effective linewidth formulas given in Ref. 8. Note that the data on which the present 10 GHz conductivity determination, $\sigma\approx0.03\ \Omega^{-1}\,\mathrm{cm}^{-1}$, is based are the same data as in Ref. 8. The 10 GHz resistivity obtained in Ref. 8 was 0.8 Ω cm. This corresponds to a conductivity which is a factor of 50 larger than the 0.03 $\Omega^{-1}\,\mathrm{cm}^{-1}$ value obtained above. This factor of 50 discrepancy in the Ref. 8 result is due to two problems. First, the Ref. 8 formulas are based on an incorrect calculation of the energy stored in the uniform mode. At 10 GHz this error contributes a factor of 10 to the discrepancy. Second, the simple analysis of Ref. 8 did not include the $S(f,H)$ factor in Eq. (38) above. At 10 GHz this $S(f,H)$ factor contributes an additional factor of 5.

[1] C. E. Patton and T. Kohane, Rev. Sci. Instrum. **3**, 76 (1972).
[2] C. E. Patton, Phys. Rev. **60**, 352 (1969).
[3] C. E. Patton, in *Magnetic Oxides*, edited by D. J. Craik (Wiley, London, 1975), p. 575.
[4] C. E. Patton, J. Appl. Phys. **1**, 1637 (1970).
[5] M. V. Kogekar and C. E. Patton, J. Magn. Magn. Mater. **54**, 1139 (1986).
[6] W. D. Wilber and L. Silber, J. Appl. Phys. **63**, 3353 (1988).
[7] K. D. McKinstry, C. E. Patton, M. A. Wittenauer, M. Sankararaman, J. Nyenhuis, F. J. Friedlaender, H. Sato, and A. Schindler, IEEE Trans. Magn. **MAG-25**, 3482 (1989).
[8] J. R. Truedson, K. D. McKinstry, R. Karim, and C. E. Patton, IEEE Trans. Magn. **MAG-25**, 3482 (1992).
[9] D. O. Smith, in *Magnetics*, edited by G. T. Rado and H. Suhl (Academic, New York, 1965), Vol. 3; p. 465.
[10] E. Schlömann, T. Kohane, and J. J. Green, Technical report AFML-TR-67-201, 1967.
[11] M. A. Wittenauer, J. A. Nyenhuis, A. I. Schindler, H. Sato, F. J. Friedlander, J. R. Truedson, R. Karim, and C. E. Patton, J. Cryst. Growth. (to be published).
[12] J. A. Osborn, Phys. Rev. **67**, 351 (1945).

Downloaded 26 Dec 2001 to 129.82.140.114. Redistribution subject to AIP license or copyright, see http://ojps.aip.org/japo/japcr.jsp

[13] H. Kojima, in *Ferromagnetic Materials*, edited by E. P. Wohlfarth (North-Holland, Amsterdam, 1982), Vol. 3, p. 305.
[14] C. E. Patton and T. Kohane, Rev. Sci. Instrum. **43**, 76 (1971).
[15] K. D. McKinstry and C. E. Patton, Rev. Sci. Instrum. **60**, 439 (1989).
[16] K. D. McKinstry, Ph.D. thesis, Colorado State University, Fort Collins, CO, 1991.
[17] J. J. Green and T. Kohane, SCP Solid State Technol. **7**, 46 (1964).
[18] J. R. Truedson, K. D. McKinstry, and C. E. Patton, IEEE Trans. Magn. **MAG-25**, 3312 (1992).
[19] J. F. Cochran, B. Heinrich, and G. Dewar, Can. J. Phys. **55**, 787 (1977).
[20] A. Yariv, *Quantum Electronics*, (Wiley, New York, 1989), p. 86.
[21] K. Zaveta, Phys. Status Solidi **2**, 2111 (1963).
[22] M. Sparks, *Ferromagnetic Relaxation* (McGraw-Hill, New York, 1964), p. 107.
[23] J. Smit and H. P. J. Wijn, *Ferrites* (Wiley, New York, 1959), pp. 229–242.
[24] R. Parker, in *Magnetic Oxides*, edited by D. J. Craik (Wiley, London, 1975), p. 439.
[25] A. K. Jonscher, Nature **267**, 673 (1977).
[26] J. R. Truedson, K. D. McKinstry, P. Kabos, and C. E. Patton, J. Appl. Phys. **74**, 2147 (1993).

Downloaded 26 Dec 2001 to 129.82.140.114. Redistribution subject to AIP license or copyright, see http://ojps.aip.org/japo/japcr.jsp